we use a thick crystal, however, it becomes difficult to observe the fringe clearly because the contribution of the second term in (4) becomes dominant. For example, a crystal thickness of 50 μm is most appropriate for observing the fringes for the 844 reflection. If a crystal 100 μm thick is used, it is quite difficult to observe the fringes.

Except very near the absorption edge, the measured f' values are in good agreement with the calculated ones (Sasaki, 1989) which take the relativistic effect into account. A similar agreement of f' values between calculation and experiment is reported for several atoms using the interferometry method (Begum, Hart, Lea & Siddons, 1986). Very near the edge, the f' values agree with the values obtained with the Parratt & Hempstead relation, which includes the damping factor.

It is noted that the errors in the determination of f' are smaller in the present approach than in the interferometry method. This is because the error estimated from (7) becomes quite small when $|f^0+f'|\simeq 0$, which is the case for the Ge 844 reflection.

In conclusion, we have shown experimentally that the *Pendellösung* fringe induced by X-ray resonant scattering is observed in high-angle reflections; it is not restricted to nearly-forbidden reflections as reported earlier (Yoshizawa *et al.*, 1988). We have also shown that the oscillations of the fringes can be used to determine the anomalous scattering factors very near the absorption edge of the atoms in a crystal. If we improve the preparation of the sample to get uniform thickness appropriate to observing the fringe, we can measure f' values within an error of 1%. Thus this approach to measuring the f' value is potentially useful, because this provides a direct method to determine f' values below the absorption edge with high precision.

The authors thank Professor K. Hayakawa of Hokkaido University for his support.

References

BATTERMAN, B. W. & CHIPMAN, D. R. (1962). *Phys. Rev.* **127**, 690-693.
BEGUM, R., HART, M., LEA, K. R. & SIDDONS, D. P. (1986). *Acta Cryst.* A**42**, 456-464.
CROMER, D. T. (1965). *Acta Cryst.* **18**, 17-23.
CROMER, D. T. & LIBERMAN, J. (1970). *J. Chem. Phys.* **53**, 1891-1898.
FUKAMACHI, T., HOSOYA, S. & OKUNUKI, M. (1976). *Acta Cryst.* A**32**, 104-109.
KATO, N. (1955). *J. Phys. Soc. Jpn*, **10**, 46-55.
KATO, N. & LANG, A. R. (1959). *Acta Cryst.* **12**, 787-794.
PARRATT, L. G. & HEMPSTEAD, C. F. (1954). *Phys. Rev.* **94**, 1593-1600.
SASAKI, S. (1989). Report 88-14 M/D, 1-136. Photon Factory, KEK, Japan.
TAKAMA, T., IWASAKI, M. & SATO, S. (1980). *Acta Cryst.* A**36**, 1025-1030.
YOSHIZAWA, M., FUKAMACHI, T., EHARA, K., KAWAMURA, T. & HAYAKAWA, K. (1988). *Acta Cryst.* A**44**, 433-436.

Acta Cryst. (1990). A**46**, 948-962

Atomic Imaging of 3:2 Mullite

BY T. EPICIER,* M. A. O'KEEFE AND G. THOMAS

National Center for Electron Microscopy, Materials and Chemical Science Division, Lawrence Berkeley Laboratory, 1 Cyclotron Road, Berkeley, California 94720, USA

(*Received 7 August 1989; accepted 17 July 1990*)

Abstract

The crystallographic structure of $3Al_2O_3$-$2SiO_2$ mullite has been studied by means of high-resolution electron microscopy. The best conditions for atomic imaging of this compound are discussed relative to the atomic resolution microscope at Berkeley. [001] multibeam images have been produced at a resolution better than 0·19 nm, allowing the cation sublattice to be directly imaged, with a firm transfer of information on the oxygen sublattice. Under optimal conditions of defocus setting and thickness, typical contrasts have been detected and consistently interpreted in terms of the presence of oxygen vacancies along the defective atomic columns. These observations are discussed in relation to the currently accepted model for the average structure of mullite.

Introduction

Mullite is an aluminium silicate mineral whose composition ranges from approximately $3Al_2O_3$-$2SiO_2$ to $2Al_2O_3$-$1SiO_2$. The ratio 'Al_2O_3/SiO_2' (designated hereafter as $[M:N]$) may be used to characterize the chemical composition of mullite whose complete formula then appears to be $Al_{4+2x}Si_{2-2x}O_{10-x}$, where x designates the number of oxygen atoms missing per

* Permanent address: INSA, GEMPPM, Bâtiment 502, associé au CNRS 341, 69621 Villeurbanne CEDEX, France.

0108-7673/90/120948-15$03.00

Table 1. *Crystallographic data for the* 3:2 *mullite* ($x = 0.25$) *compiled from the literature and used in the present work* (*the designation of the Wyckoff positions is given between parentheses in the second column*)

The occupancy factors tend to conform to the following general relationships over the whole compositional range: occupancy $= 1 - x/2$ for T(Al+Si) sites; occupancy $= 1 - 3x/2$ for O3 sites; occupancy $= x/2$ for O* and T^* (Al+Si) sites.

Space group *Pbam*, $a = 0.754$, $b = 0.768$, $c = 0.2885$ nm.

	Designation	x	y	z	Occupancy	Debye-Waller (nm^2)
Al	Al1(2*a*)	0	0	0	1·0	0·0045
Al	*T*(4*h*)	0·351	0·159	0·5	0·54	0·0054
Si	*T*(4*h*)	0·351	0·159	0·5	0·33	0·0054
Al	*T**(4*h*)	0·236	0·294	0·5	0·1	0·005
Si	*T**(4*h*)	0·236	0·294	0·5	0·03	0·005
O	O1(4*g*)	0·374	0·283	0	1·0	0·01
O	O2(4*h*)	0·139	0·076	0·5	1·0	0·01
O	O3(2*d*)	0	0·5	0·5	0·63	0·01
O	O*(4*h*)	0·053	0·447	0·5	0·13	0·01

average unit cell; relations between x and $[M:N]$ are

$$x = 2\frac{[M:N]-1}{2[M:N]+1} \quad \text{and} \quad [M:N] = \frac{1+x/2}{1-x}. \quad (1)$$

Most interest concerning mullite arises from the fact that this compound is a potential candidate for high-temperature applications in the ceramic-materials field. Moreover, the exact crystallography of mullites, depending upon the $M:N$ ratio, is still the subject of refinement. Both aspects have led us to undertake a structural characterization of various 3:2 mullites by means of high-resolution electron microscopy (HREM). It will be shown in this paper that mullite can be atomically imaged at a resolution better than 0·2 nm, using the atomic resolution microscope (ARM) at the NCEM; this has made it possible to examine at a very local scale the atomic reorganization occurring around oxygen vacancies, which appear to be randomly distributed in the studied compounds.

Crystallographic background

The structure of mullite has been studied by many authors and is well documented throughout the literature (Angel & Prewitt, 1986; Burnham, 1963, 1964; Cameron, 1977; Saalfeld & Guse, 1981; Sadanaga, Tokonami & Takeuchi, 1962; Tokonami, Nakajima & Morimoto, 1980). It consists of octahedral AlO_6 chains parallel to the c axis and cross linked by tetrahedral $(Al, Si)O_4$ chains (see Table 1 and Fig. 1 for details).

Owing to the presence of some oxygen vacancies on O3 sites (Fig. 1*c* and Table 1), one has to deal with the average cell shown in Fig. 1(*a*), rather than the perfect cell depicted in Fig. 1(*b*). For Al-rich mullite ($x \geq 0.40$, *i.e.* compositions near $M:N = 2:1$), both X-ray (Angel & Prewitt, 1987; Saalfeld, 1979; Tokonami, Nakajima & Morimoto, 1980) and electron (Cameron, 1977; Kriven & Pask, 1983; Nakajima & Ribbe, 1981; Smith & McConnell, 1966) single-crystal diffraction patterns exhibit diffuse or sharp superstructure reflections which indicate a tendency for the ordering of the vacancies. These superstructures have recently been explained in terms of a symmetry analysis for incommensurate modulated structures (McConnell & Heine, 1985). HREM has been used to reveal directly the ordered microstructure of such compounds: 'superstructure images' have been produced by including only superlattice beams in the objective aperture, and sets of white dots, associated with the presence of vacancy

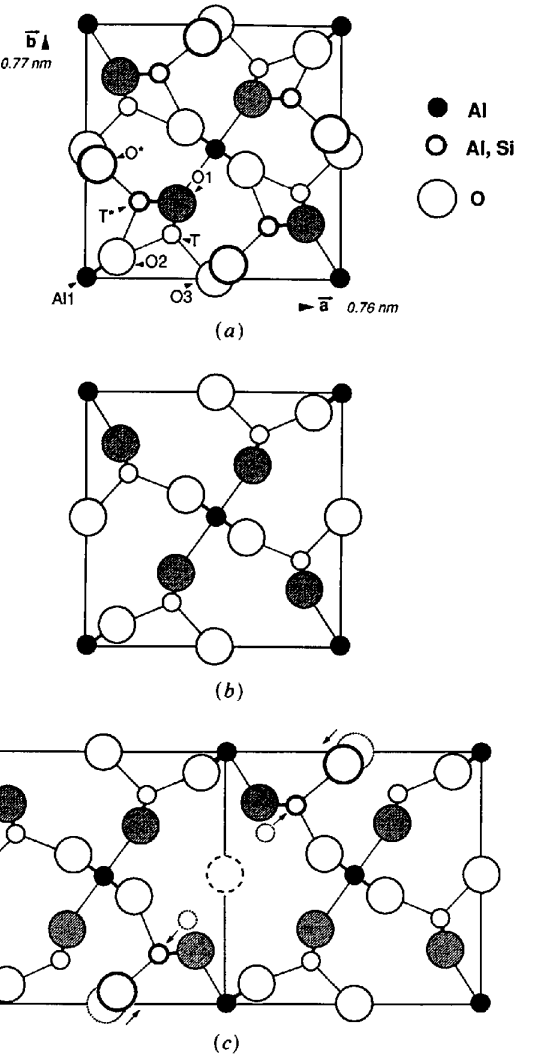

Fig. 1. [001] projections of the structure of mullite. (*a*) Average unit cell. Heavily outlined sites have partial occupancies and represent displaced atoms due to the presence of oxygen vacancies (*c*). Dark and shaded atoms are those located at $z = 0$; (*b*) perfect structure of mullite, *i.e.* in the hypothetical case where there is no oxygen vacancy; (*c*) model of atomic displacements around a vacancy on an O3 site (displacements, indicated by arrows, allow the atoms of interest to be almost correctly recoordinated).

columns, have been imaged in the [010] orientation (Nakajima, Morimoto & Watanabe, 1975; Yla-Jaaski & Nissen, 1983).* Such observations do not, however, allow atomic displacements around individual vacancies (Fig. 1*c*) to be resolved, because of insufficient resolution under the conditions used by these authors. 'Structure imaging' has recently been attempted (Schryvers, Srikrishna, O'Keefe & Thomas, 1988) in [001] orientation on a $1{\cdot}7Al_2O_3$–$1SiO_2$ mullite; although reliable, their observations do not allow the structure to be imaged at an acceptable resolution in order to discuss the previous point. The present work was then undertaken to examine the conditions under which the structure of mullite can be correctly imaged in HREM and, consequently, to check the atomic displacements previously refined by macroscopic diffraction techniques.

Note added in proof

We note that a recent attempt to interpret vacancy distributions in mullite using simulated images (Hamid Rahman & Weichert, 1990) is flawed due to an incorrect method of modelling an isolated vacancy (Epicier, Thomas & O'Keefe, 1991).

Experimental

1. *Specimen*

Two types of polycrystalline 3:2 mullites have been used in the present investigation. The first one (labelled *K* hereafter) is from the Kyocera company, and the second one (*T*) has been sintered from the Baikowski 193 CR starting powder (Torrecillas, 1987). The composition has been ascertained in both cases by chemical analysis in the microscope as described below.

Thin foils adequate for transmission electron microscopy have been conventionally prepared by ion-beam thinning (5·5 kV argon beams, incidence angle 30 °); a carbon coating was performed in order to avoid charging under the electron beam.

2. *Chemical analysis*

Chemical analysis of the samples was achieved on a JEOL 200 CX microscope, equipped with an ultra-thin window detector and a Kevex 8000 Analyst. Data obtained by a simultaneous analysis of oxygen, aluminium and silicon in several grains were consistently interpreted and final results with maximum error of 0·5 wt% are:

K sample: Al_2O_3: 73·3 wt%; SiO_2: 26·7 wt%,

i.e. $[M:N] = 3{\cdot}30/2{\cdot}00$ ($x \simeq 0{\cdot}30$);

T sample: Al_2O_3: 71·5 wt%; SiO_2: 28·5 wt%,

i.e. $[M:N] = 3{\cdot}00/2{\cdot}00$ ($x = 0{\cdot}25$).

Impurities were not detected in the mullite grains of any of these compounds.

Table 2. *Experimental and computing data for the HREM work*

Accelerating voltage	800 kV
Spherical aberration coefficient C_s	2 mm*
Spread of focus	15 nm*
Semi-angle of beam convergence	0·8 mrad†
Objective aperture radius	8·9 nm^{-1}
Maximal spatial frequency for multislice	20·0 nm^{-1} (625 beams)
Maximal spatial frequency for phase grating	40·0 nm^{-1} (2500 coefficients)
Thickness of the elementary slice	0·2885 nm (|c|)
Crystallographic data	See Table 1‡

* In agreement with actual values determined (Hetherington, Nelson, Westmacott, Gronsky & Thomas, 1989). Under such conditions, the 'point resolution' of the microscope appears to be limited to ~0·16 nm, due to chromatic error and residual vibration (the 'Scherzer resolution limit' would be around 0·14 nm).

† Experimentally measured on diffraction patterns.

‡ Readjustment of occupancy factors - according to the relations given in Table 1 - has been done for the *K* mullite, for which *x* (0·30) differs slightly from the ideal value (0·25).

3. *HREM observations*

The high-resolution study was conducted on the atomic resolution microscope (JEOL ARM-1000) at the NCEM. The operating conditions, as well as the required data for computer multislice simulations using both *SHRLI* (O'Keefe & Buseck, 1979) and *CEMPAS* (Kilaas, 1987) packages are summarized in Table 2.

Observations were limited to the [001] orientation, since it was checked by preliminary calculations that other low-index azimuths do not allow the structure to be imaged at a sufficient resolution.

Extensive 'through-focus series' were recorded in order to ascertain the structure through the examination of several consistent images; defocus values were deduced from the manufacturer's calibration of the focusing controls, and also directly estimated from the analysis of diffractograms from amorphous regions on an optical bench. Occasional digitizing of the micrographs at a resolution of 2048 by 2048 pixels with an Eikonix 78/99 camera controlled by a locally written command incorporated into the *SEMPER* programs of Saxton, Pitt & Horner (1979) was performed for numerical treatment and improvement of the experimental images by spatial filtering.

* Details about the so-called 'superstructure imaging' in HREM may be found in the paper of Hiraga, Shindo & Hirabayashi, (1981); a specific study concerning imaging of ordered carbon vacancies in a sub-stoichiometric carbide, which may serve as a generic example for imaging the ordered distribution of vacancies on a light-element sublattice, has also recently been reported by Epicier, Fuchs, Ferret & Blanchin (1989).

Results

1. *Required resolution for 'structure imaging' of mullite*

In order to know the range of information available at a given experimental resolution, a set of calculations of 'weak-phase-object' (WPO) images has been carried out. Fig. 2 shows these images as projections of the crystal-structure potential to the resolutions indicated. From these theoretical images, it clearly appears that (provided one obtains a suitably thin specimen) an experimental resolution of at least 0·19 to 0·17 nm is needed to detect the presence of oxygen around cations under Scherzer defocus conditions (*i.e.* while attempting to image simultaneously the cation sublattice). Also, it is seen that a 0·24 nm resolution is insufficient to achieve this goal; this latter resolution corresponds to that available on current 100 or 200 kV microscopes such as those used in the earlier high-resolution microscope investigations of mullite (Nakajima, Morimoto & Watanabe, 1975; Yla-Jaaski & Nissen, 1983; Eberhard, Hamid Rahman & Weichert, 1986). Ideally, a 0·12 nm resolution, which has not yet been experimentally obtained on any existing microscope, would be required for separating both cation and anion atomic columns (Fig. 2).

2. *Best experimental conditions for atomic imaging of mullite*

From the above, the demonstrated resolution of the ARM (<0·17 nm, as indicated in Table 2) is

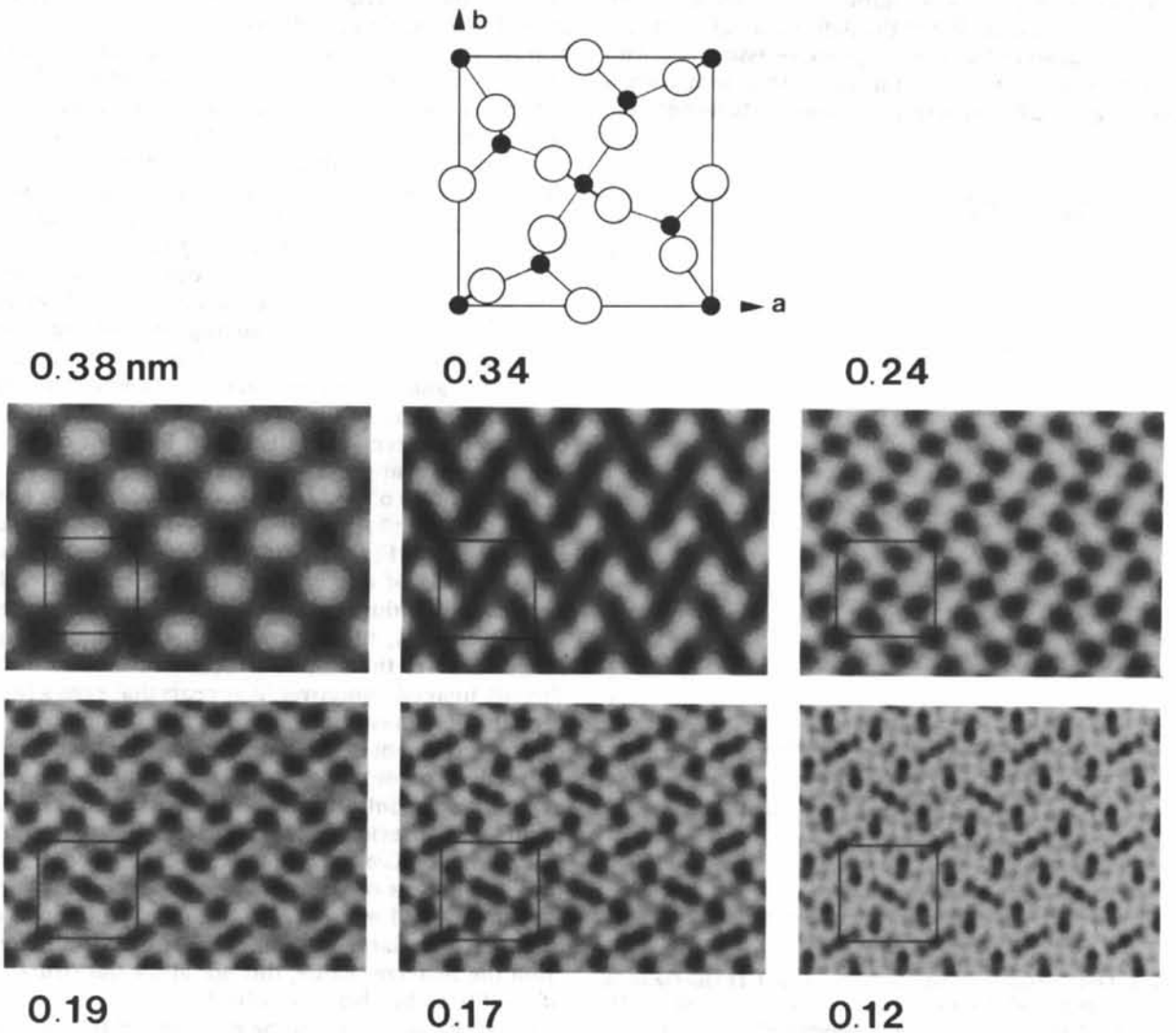

Fig. 2. Weak-phase-object images of mullite for increasing resolution (marked in nm). A unit-cell position is marked on each image for comparison with the perfect cell drawn above. A resolution of at least 0·19 nm is required to detect the presence of the anions, and 0·12 nm is required to resolve them completely.

adequate for transferring actual image information on the oxygen atoms (and vacancies) in the case of mullite. However, the peculiarities of the contrast transfer function (CTF) of the ARM make it worth examining in detail the setting of the focusing conditions for optimal imaging of the structure of mullite. Fig. 3 reproduces CTF plots for two defocus values of particular interest, Δf_1 and Δf_2, respectively equal to -55 and -80 nm (where underfocus is assigned negative values) and roughly corresponding to $n = 1$ and 2 in the following formula:

$$\Delta f_n = -[(3n/2)C_s\lambda]^{1/2}$$

(λ is the electron wavelength, *viz* 0·00102 nm at 800 kV).

Owing to the particular shape of the damping envelope caused by chromatic aberration, it is seen in Fig. 3 that the setting of the defocus to Δf_2 provides a better transfer of spatial frequencies associated with distances in the 0·2–0·17 nm range than that corresponding to Δf_1 (Scherzer defocus). Moreover, the

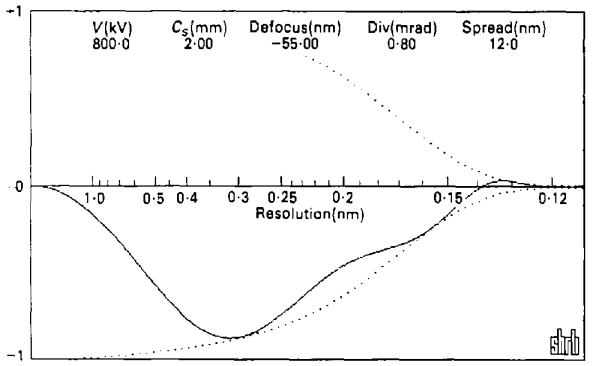

(*a*)

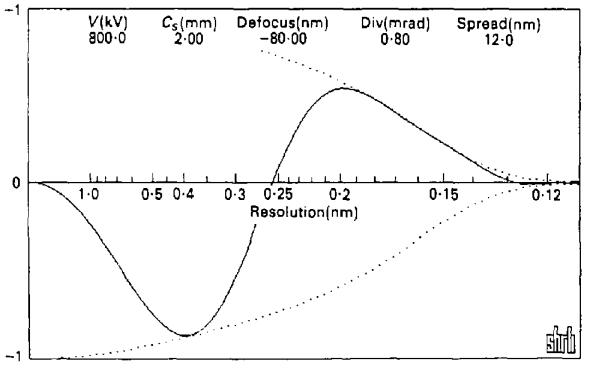

(*b*)

Fig. 3. Linear-image contrast transfer function (CTF) for the JEOL ARM-1000 at 800 kV. (*a*) Scherzer defocus $\Delta f_1 = -55$ nm; (*b*) $\Delta f_2 = -80$ nm. At Δf_2, maximum transfer is obtained in the 0·20 to 0·17 nm range since the CTF (solid line) lies hard against the chromatic aberration damping curve (dashed line). At Δf_1 some potential transfer is lost because the CTF does not lie along the damping curve.

CTF zero near the 4 nm^{-1} frequency (corresponding to 0·25 nm spacings) will probably lead to an improvement of the signal-to-noise ratio, since undesirable information due to contamination is generally expected to be transferred in the 0·20–0·25 nm range. Then, Δf_2 should be preferred for imaging details below 0·2 nm. Unfortunately, it is seen that the setting at Δf_2 gives rise to a sign inversion for frequencies associated with distances respectively higher and lower than $d_0 \simeq 0{\cdot}26$ nm: in the classical WPO approximation (Spence, 1980), this would lead to dark contrast for atomic columns at the intersection of lattice fringes of inter-reticular distances higher than d_0, and white contrast otherwise. When dealing with mullite, it appears that this situation will not allow better images to be obtained by using Δf_2, although this setting permits a better transfer of the highest spatial frequencies. This is clearly demonstrated in Figs. 4 and 5. As will be seen below, it also appears that Δf_1 is the best defocus value for obtaining multibeam images with the finest scale of details.

Further questions may be posed about the influence of lens-focus setting on the quality of high-resolution micrographs of mullite. Fig. 6(*a*) shows a set of calculated images at different defocus values for a reasonably low thickness (these images are calculated from the structural model of Fig. 1*a*).

The 'best' types of image are only obtained near the Scherzer defocus as experimentally observed (Fig. 4). The experimental micrographs of Fig. 6(*b*) are from wide through-focus series which are self-consistent and exhibit excellent agreement with the simulated images of Fig. 6(*a*). As already mentioned, the resolution remains rather poor for most defocus values, except at the Scherzer defocus.

Examination of wedge-shaped crystals reveals how the thickness influences the contrast of experimental images. From Fig. 7, it is seen that the 'structure image' aspect of the micrographs is already severely perturbed for thicknesses as low as $t_2 = 8$ nm. For thicker crystals, the Scherzer defocus condition no longer enables the atomic structure of mullite to be directly imaged; moreover, it appears that even a little crystal tilt (unavoidable in practice, even with a careful alignment of the zone axis in the selected-area diffraction mode) has a drastic influence on the experimental contrast as can be seen in Fig. 7(*c*). This point was previously investigated by Schryvers, Srikrishna, O'Keefe & Thomas (1988). However, the present analysis of thickness and tilt effects explains why their ARM micrographs, frequently obtained at thicknesses as large as 8 nm, and at defoci different from the Scherzer value, did not allow the structure of mullite to be clearly resolved.

From the above, it can be pointed out that atomic imaging of mullite can be successful only on very thin crystals (less than 6 nm nominally) at the Scherzer defocus condition.

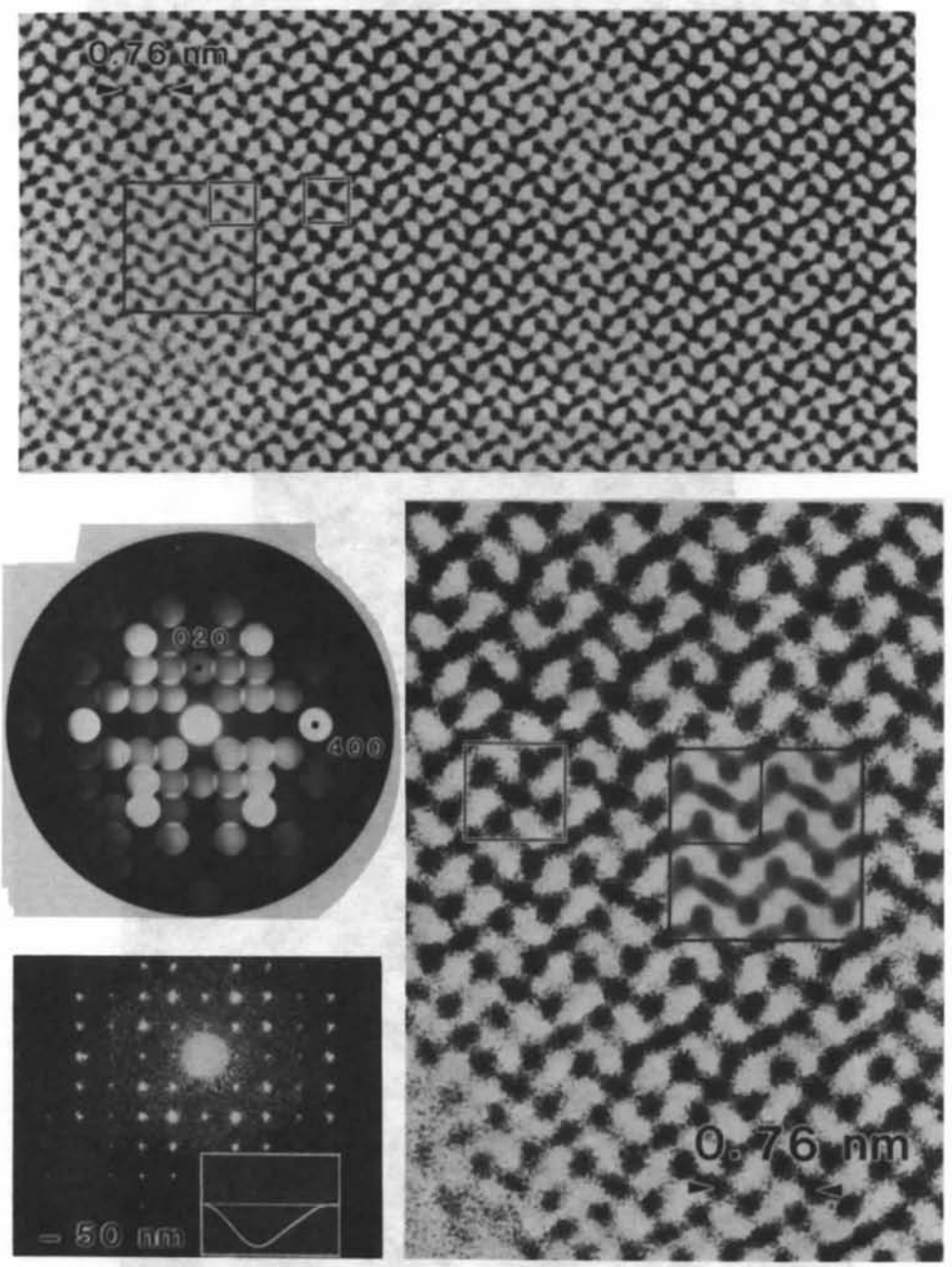

Fig. 4. Experimental Scherzer micrograph of T mullite; the inset simulated image corresponds to $t = 2{\cdot}3$ nm and $\Delta f = -50$ nm (note the correspondence with the 0·19 nm WPO image in Fig. 2). The diffraction pattern shows the incident-beam convergence under imaging conditions. The diffractogram shows the spatial frequencies contributing to the image, in particular the strong 0·19 nm contribution from the 400–000 interference. The inset CTF shows that frequencies much beyond 0·19 nm are severely damped.

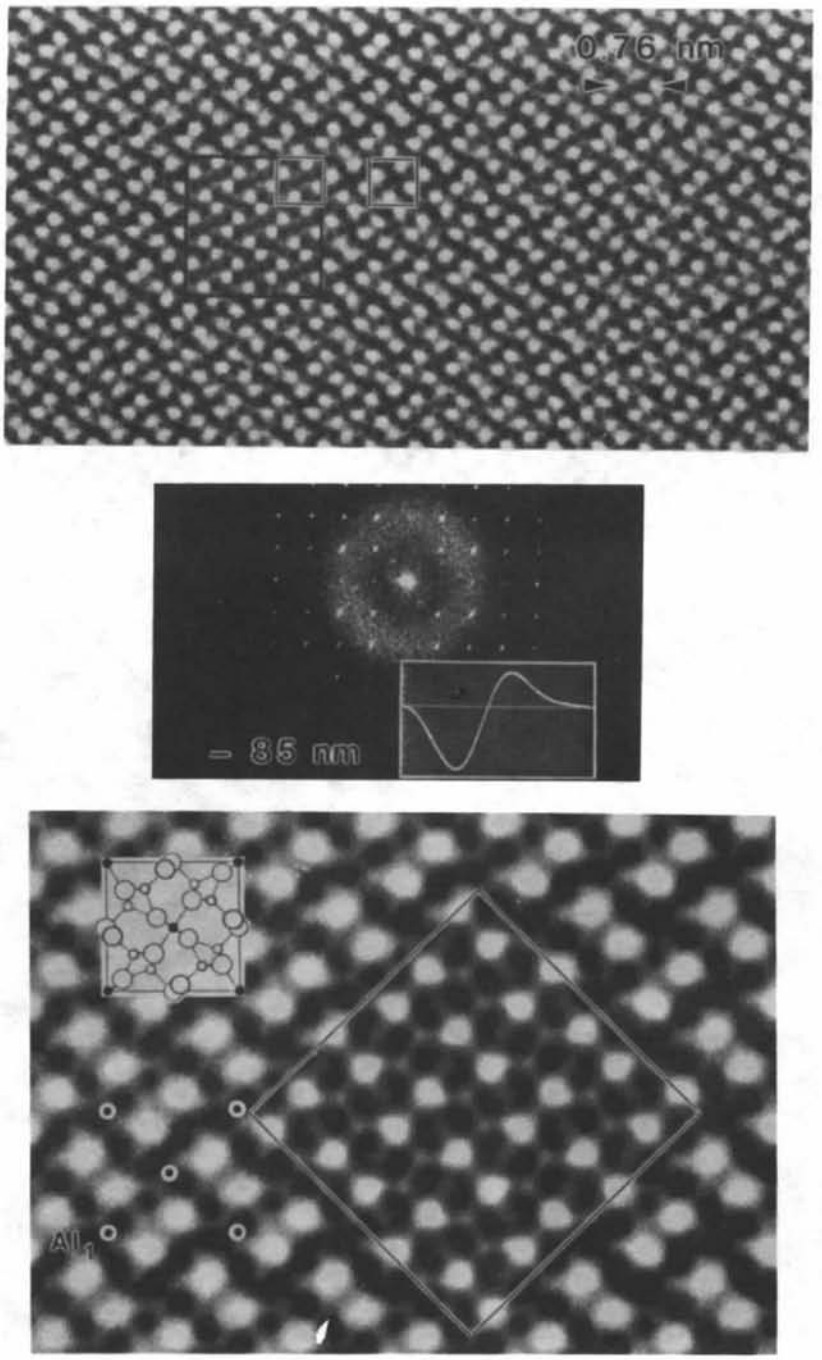

Fig. 5. Images of T mullite at a defocus near Δf_2 (the experimental defocus value estimated from the diffractogram is −85 nm). The image at the bottom has been digitized and processed in order to improve image quality. Inset calculated images correspond to $t = 3$ nm and $\Delta f = -85$ nm; the identification of the aluminium columns (marked) is somewhat tedious, due to the effect of the CTF illustrated by Fig. 3.

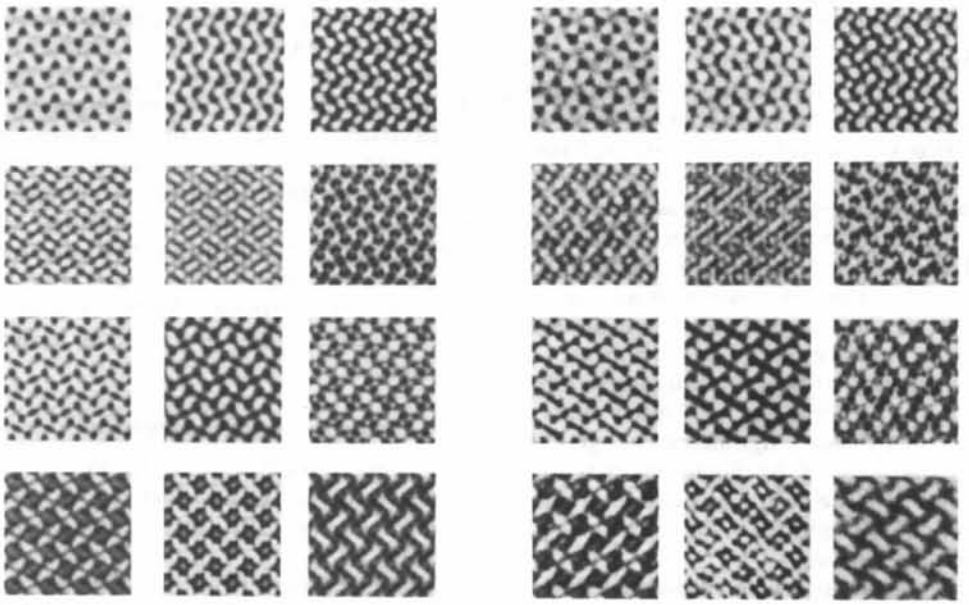

(a) (b)

Fig. 6. (*a*) Matrix of calculated images for a reasonably low thickness and different defoci (from left to right and top to bottom: Δf (nm) = +70, +45, +30, +10, 0, −20, −40, −60, −90, −100, −110 and −140); (*b*) experimental through-focus series from the *T* mullite corresponding to (*a*).

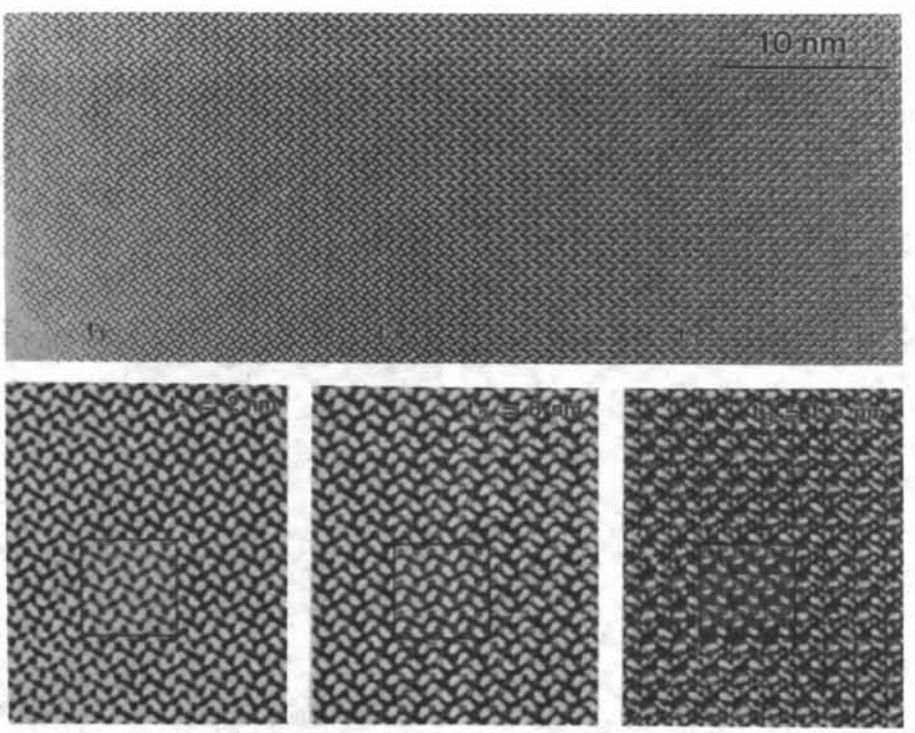

Fig. 7. Influence of specimen thickness on images of mullite at Scherzer defocus (*T* mullite). Image contrast at positions marked t_1, t_2 and t_3 was matched by image simulations at thicknesses of 2, 8 and 16 nm respectively (insets). The contrast obtained at $t_3 \simeq 16$ nm is slightly modified by crystal tilt (the calculated image corresponds to a 1·9 mrad tilt in the [110] direction; however, the match is not perfect due to the extreme difficulty of determining the actual misorientation with a sufficient accuracy, even through optical or numerical diffractogram analysis).

3. *Artefacts due to microscope misalignment*

Among the various adjustments that have to be done for atomic-resolution imaging, beam alignment in the objective lens and correction of objective-lens astigmatism are of critical importance (Smith, Saxton, O'Keefe, Wood & Stobbs, 1983).

The special tilt-alignment device available on-line on the ARM (Hetherington, Nelson, Westmacott, Gronsky & Thomas, 1989) enables the operator to set the beam parallel to the optic axis with an accuracy of about 0·5 mrad. This angle is less than the semi-angle of beam convergence, $\theta_c = 0{\cdot}8$ mrad. An academic investigation of beam misalignment effects reveals that a tilt as large as ~2·5 mrad must be considered in order to see a significant change in the experimental contrast (Fig. 8). Such misorientations are much greater than the accuracy mentioned above, and this effect can be ignored if the alignment procedure is normally followed.

Astigmatism corrections were performed through the usual method based on the refinement of the 'zero contrast' focusing of the amorphous edge. However, a major problem appeared when this contamination layer was insufficient (Fig. 9*a*), since astigmatism correction based directly on the aspect of the crystal image appeared to be extremely delicate, due to the lack of simple symmetries in the correctly adjusted Scherzer image (Fig. 4). It appeared that a good adjustment was possible by underfocusing the image in order to obtain the almost perfect fourfold symmetric images shown in Fig. 6 for defoci ranging between −80 and −130 nm nominally. It must be noticed that even a low value of astigmatism produced a tremendous change in image contrast (Fig. 9*b*), making any interpretation meaningless, and even inviting dangerous false conclusions, since the predominant white dots in Fig. 9(*b*) due to astigmatism might, according to the literature (Yla-Jaaski & Nissen, 1983; Epicier, Fuchs, Ferret & Blanchin, 1989), suggest the presence of ordered vacancy columns.

4. *Detection of oxygen vacancies*

The micrographs reported in Fig. 10 show a reliable analysis of the structure of the 3:2 mullite for the case of sample *K* (see caption for detailed comments).

As can be seen from the regions arrowed in Fig. 10(*a*), typical defect contrasts have been detected, which will be shown to be consistent with the presence of oxygen vacancies within the crystal. Extensive calculations (summarized in Fig 10*e*) show how a good description of these defects has been realized assuming the existence of half-vacant oxygen columns in the foil. Considering the low thickness of the examined area, this corresponds to the presence

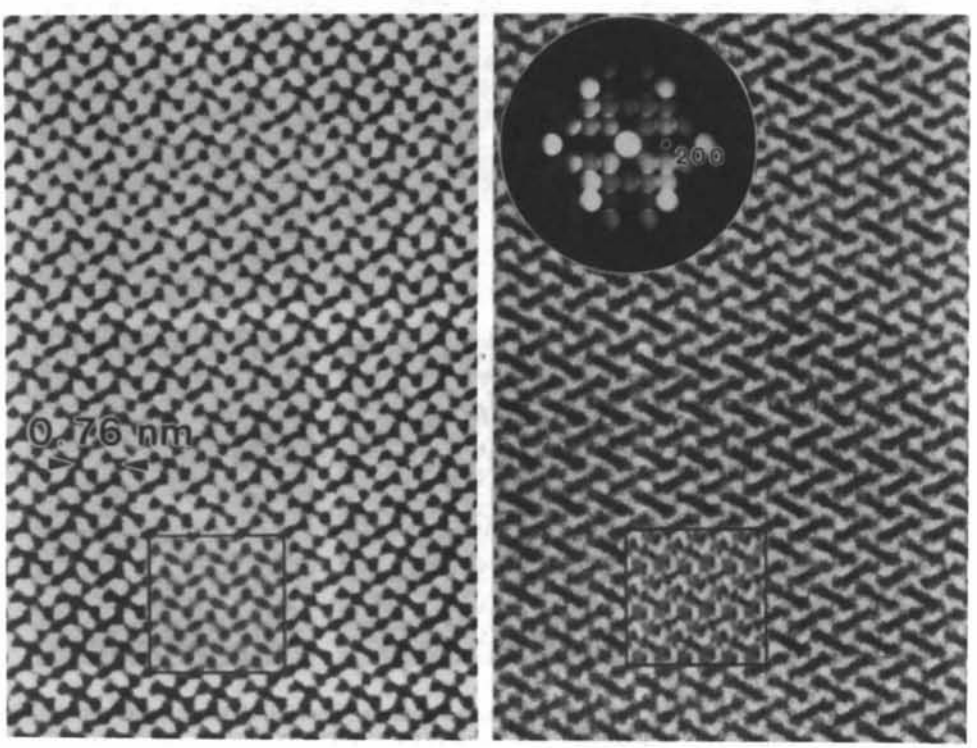

Fig. 8. Effect of beam tilt (right) on the Scherzer image (left) of a 3 nm thick *T* mullite crystal [tilt is approximately 2·7 mrad, corresponding to the beam aligned on (200); see inset diffraction pattern].

of two to four vacancies along the defective atomic rows. The apparently random distribution of such defects strongly supports the commonly accepted hypothesis that oxygen vacancies are disordered in the 3:2 compound. Furthermore, conventional electron diffraction analysis of the samples gave no evidence for superlattice reflections.

Moreover, it can be said that there is no hope of resolving the presence of any single point defect, since, according to images simulated for columns containing mixtures of vacancies and perfect structure, vacancy occupancies lower than about 0·5 do not give rise to any detectable contrast (Fig. 11). It is also clear that the average structure of Fig. 1(*a*) describes correctly the crystal in most areas, except in those where the random distribution of vacancies is such that the occupancy of displaced T^*-type columns becomes higher than 0·5.

To interpret the defect contrast observed in Fig. 10(*d*), multislice simulations have been carried out for a wide range of vacancy contents along the defect column. Using an option to stack different elementary slices in the multislice calculations, several thin foils consisting of intercalated 'perfect' cells (such as the one shown in Fig. 1*b*) and 'imperfect' ones [corresponding to the model of Fig. 1(*c*)] have been constructed. For computational reasons, we have used a four by four supercell in each case, which also allows the result to be untroubled by artefacts arising from the borders of the cells (the actual size of the supercell was then 3·02 by 3·07 nm). In so doing, we were actually able to describe physical stacking sequences. Depending on the total number of stacked cells, it was obviously not possible to increase the vacancy content continuously from 0 to 1, but particular values could be obtained while increasing the vacancy number from 0 to the total number of sites available in a column of any given thickness.

Fig. 11 is a matrix of calculated images for the three defocus values experimentally obtained (Fig. 10*d*). In order to check the sensitivity of the defect contrast with respect to the thickness, calculations were run for three reasonable thicknesses for which the perfect average cell of Fig. 1(*a*) matches the experimental images very well. These simulations can be analysed using three distinct features which are visible in Fig. 12(*a*), and described below.

Feature 1: for a high vacancy content, the parallel straight lines defined by the black dots imaging cations around the defect columns become curved and are displaced away from each other in the image at −50 nm defocus.

Feature 2: under the same vacancy conditions, but at −87·5 nm defocus, the white dots associated by pair and located at the emplacement of the defective O3-type column in the greatest underfocused images

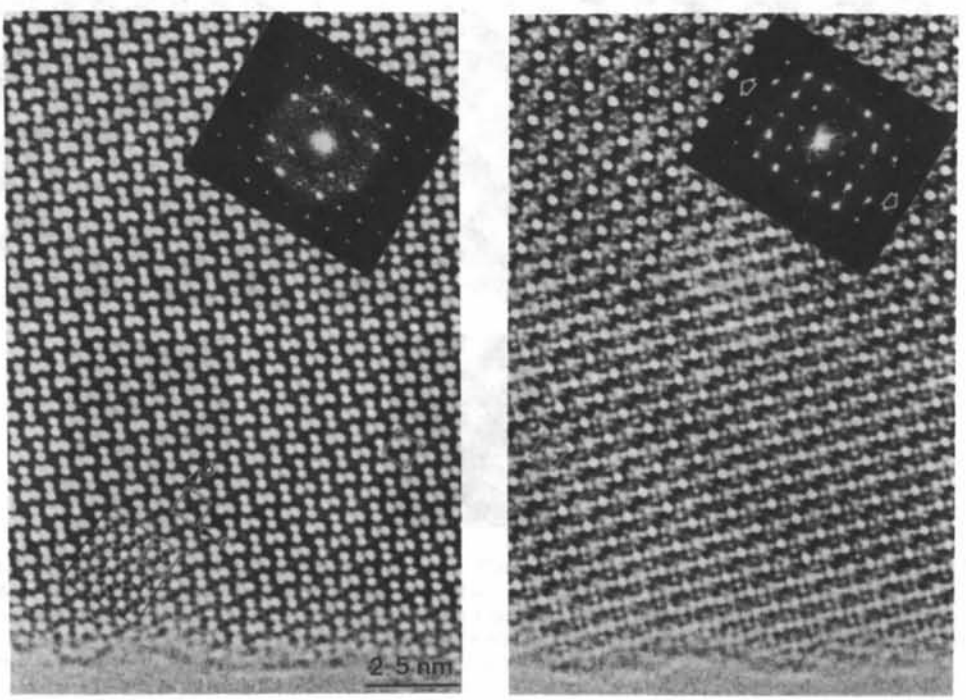

(*a*) (*b*)

Fig. 9. Effect of astigmatism on HREM micrographs of T mullite. (*a*) Acceptable astigmatism correction, as revealed by the inset diffractogram (obtained from a close area where a contamination layer is present, contrary to the shown region, which exhibits a very clean edge); t and Δf are 3 nm and −80 nm respectively for the calculated image. (*b*) Incorrect astigmatism setting.

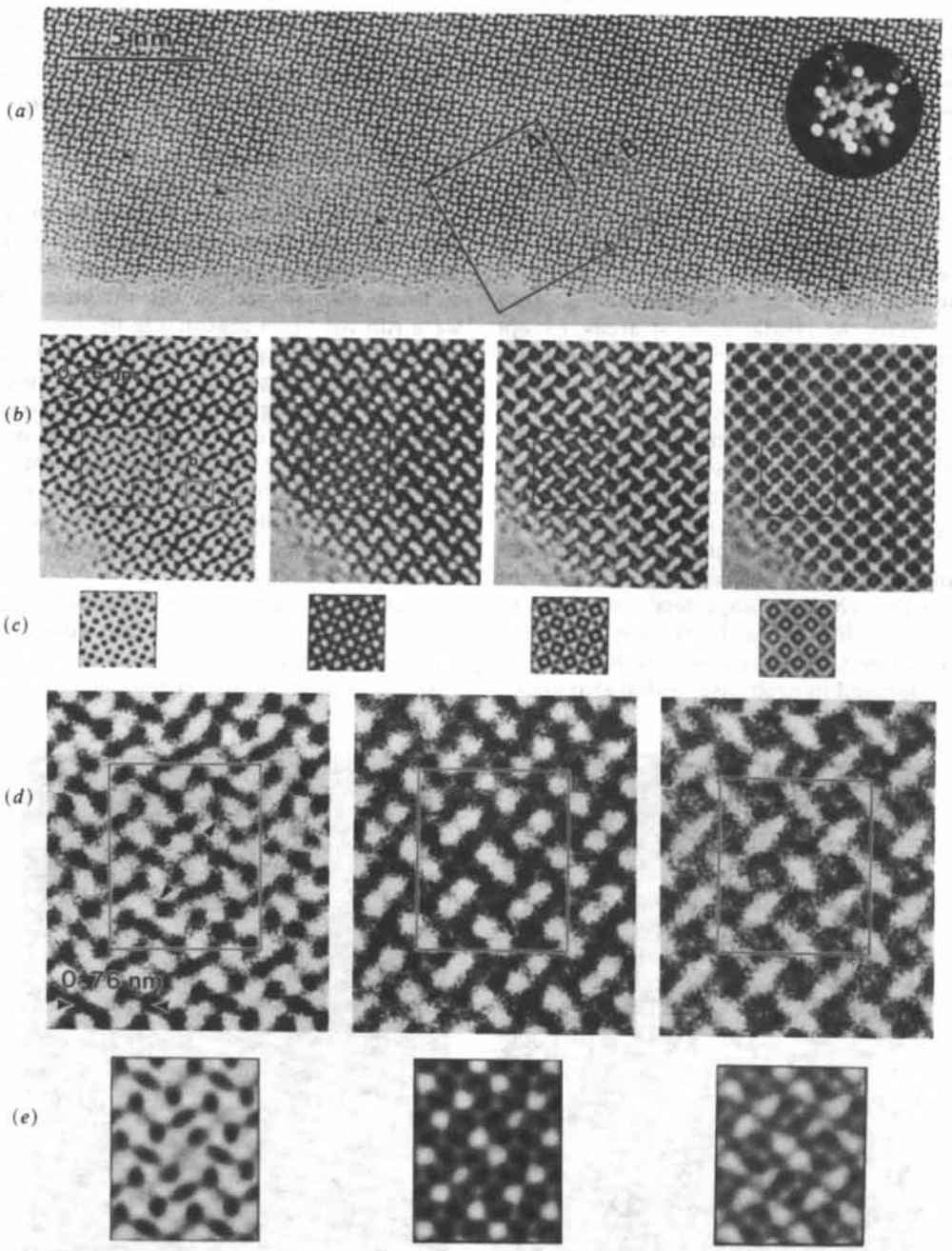

Fig. 10. HREM analysis of a thin uniform crystal edge in *K* mullite. (*a*) Low-magnification micrograph taken at Scherzer defocus (−50 nm); details *A* and *B* are examined in (*b*) and (*d*), respectively; arrows indicate similar defects to the one studied in (*d*). (*b*) Through-focus series from detail *A* in (*a*) [from left to right: Δf (nm) = −50, −87·5, −97·5, −117·5; the thickness used in the inset calculated images is 1·4 nm, but identical contrasts are obtained within ±0·5 nm]. (*c*) Corresponding calculated images for a hypothetical structure where oxygen atoms are missing (without any atomic displacements); note the disagreement with experimental images in (*b*). (*d*) Enlargement of detail *B* for three defoci (−50, −87·5 and −97·5 nm); arrows in the first micrograph indicate a distortion of triplets of dark dots. (*e*) Calculated images matching the previous experimental micrographs; they correspond to a 1·16 nm thin crystal with two vacancies along the central O3-type oxygen column, according to the model of Fig. 1(*c*).

clearly become closer and brighter than in the perfect-crystal image.

Feature 3: in the images at −97·5 nm defocus, and for vacancy contents approaching 1, the white dots close to the defect and aligned parallel to the direction of displacement in feature 1 become diffuse and elongated.

These three particular features allow acceptable ranges of vacancy content to be assigned to the experimental images; clearly, concentrations lower than 0·4 nominally (the lower two images in each column of Fig. 11) cannot fit the micrographs of Fig. 10(*d*), since they do not lead to a detectable contrast for feature 1. Similarly, feature 3, which is not observed experimentally, allows the highest vacancy contents, above 0·8 nominally, to be eliminated. All things considered, a compromise agreement is obtained for all three features if we assume a vacancy content of around 0·5, whatever the thickness. The case of 0·5 vacancy content for a low thickness of 1·16 nm (*i.e.* two vacancies along the four-cells long [001] column) has been reproduced with an adjusted contrast in Fig. 10(*e*).

Further remarks need to be made to complete this analysis. As deduced from Fig. 12(*b*), it is clear that the defect contrast is mainly due to the displacement

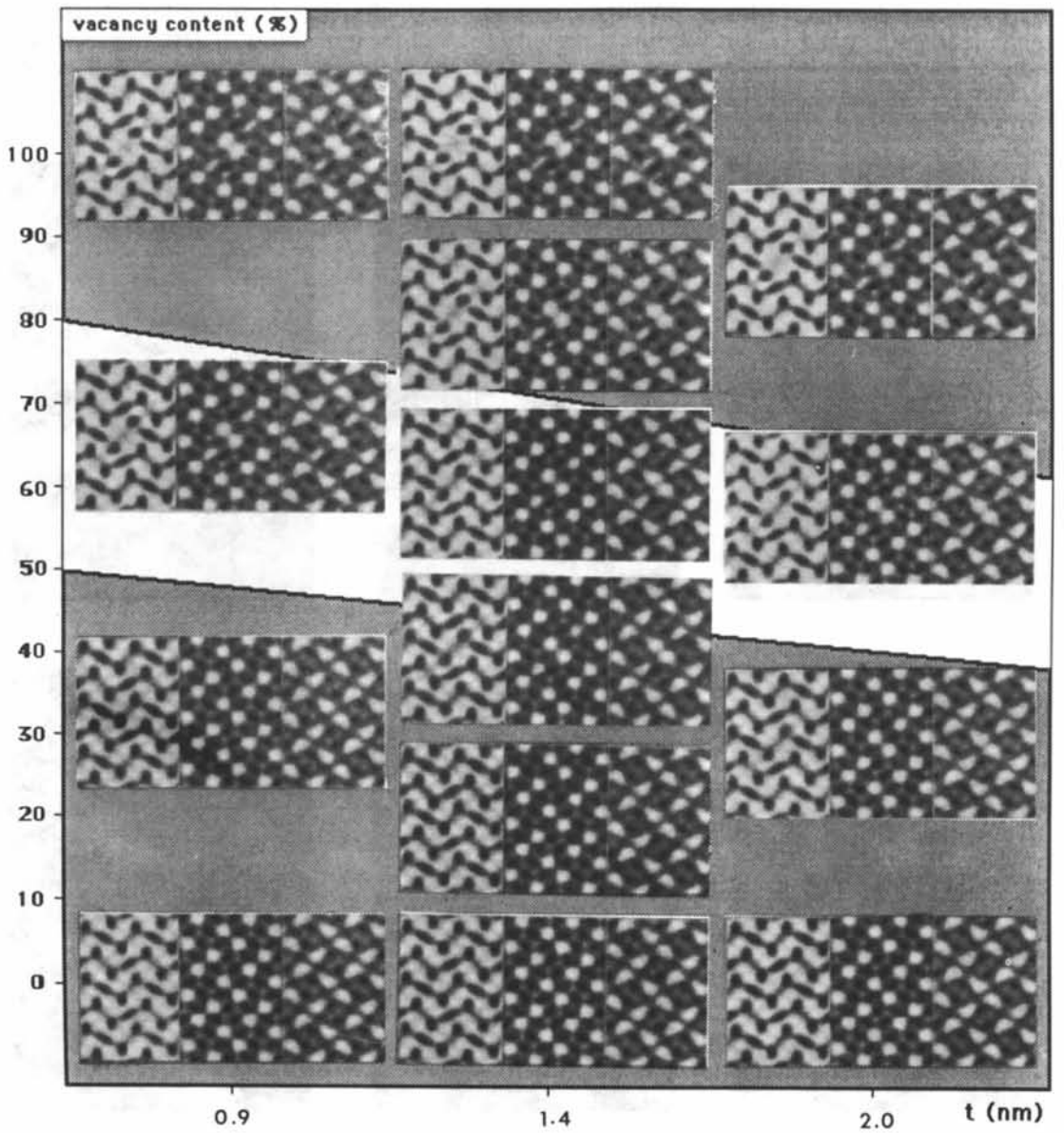

Fig. 11. Matrix of calculated images of a defect crystal containing various numbers of oxygen vacancies along an O3-type column, according to the model of Fig. 1(*c*) (see text). The three images in each group correspond to the defocus values determined for the experimental images of Fig. 10(*d*). Groups of images are shown for three values of crystal thickness (marked).

of metallic atoms, rather than to the vacancies themselves. From the above, we can conclude that oxygen vacancies can be detected if at least half of the metallic atoms along each of the T-type columns close to a defective O3-type column have been displaced into T^* sites (Fig. 1).

An elementary numerical approach allows the probability $p(\tau, t)$ for having at least a fraction τ of metallic atoms displaced (due to the presence of τ vacancies on the O3 first-neighbour site) along a T-type column of thickness t to be calculated under the assumption of a random distribution of the oxygen vacancies (that is, according to the data from Tables 1 and 2, an average occupancy factor of $1-x/2$ for the T sites, or 0·85 in the case of the K mullite).

The results are shown in Fig. 13. The full-line curve corresponds to the general case where no restriction applies to the way vacancies are distributed along the defect column; for a crystal thickness varying from 0·87 to 3 nm, $p(0{\cdot}5, t)$ decreases from 21 to ~8%, indicating a relatively low probability of detecting defective O3-type columns. However, it is strongly believed that this situation is not realistic: a totally random distribution allows two vacancies to be in first-nearest-neighbour positions at z_0 and $z_0+|\mathbf{c}|$ along an O3-type column. Previous HREM results on ordered mullite near the 2:1 composition suggest that vacancies avoid the nearest-neighbour positions, since they always appear to be separated by at least a fully occupied O3 site along the c axis (Nakajima, Morimoto & Watanabe, 1975; Yla-Jaaski & Nissen, 1983). Adding this constraint to the random distribution leads to the dashed curve in Fig. 13, which clearly shows that the probability of detecting oxygen vacancies is then considerably lowered, since it now remains below 1·4% for thicknesses larger than 3 nm. It is

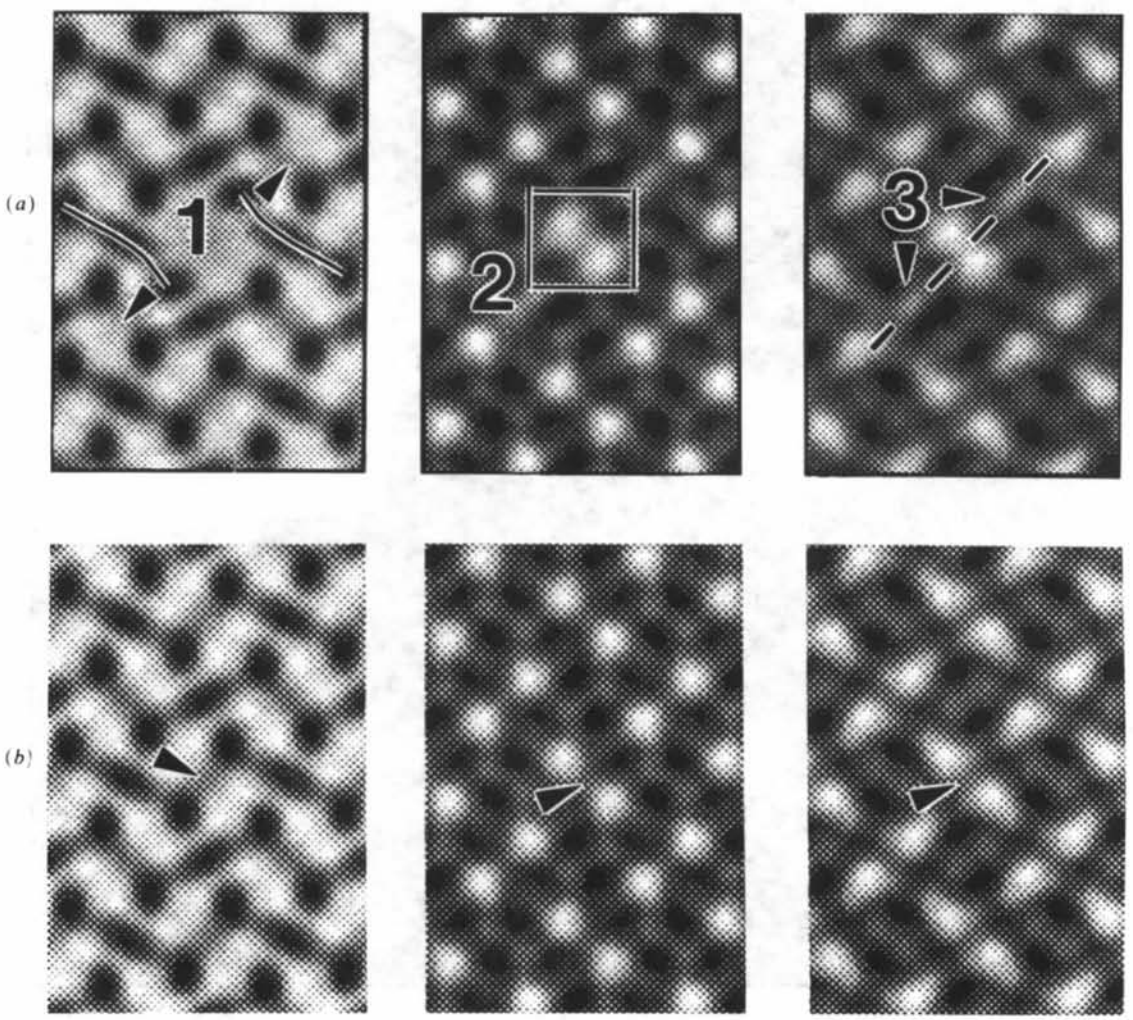

Fig. 12. (*a*) Drawings showing the three features allowing consistent analysis of Figs. 10(*d*)-(*e*) and 11 (see text). (*b*) Hypothetical contrast produced by the presence of a vacant O3-type column (arrow) without atomic displacement: no defect can be detected ($t=1{\cdot}4$ nm, $\Delta f=-50$, $-87{\cdot}5$ and $-97{\cdot}5$ nm, respectively).

believed that this situation might describe the experimental observations reported in Fig. 10 on the *K* mullite.

Moreover, no matter which restrictions are applied to the actual distribution of vacancies, it is clear from Fig. 13 that the probability of detecting defective columns rapidly approaches zero for thicknesses larger than 3 nm nominally; this explains why no defect contrast is experimentally discerned for thick crystals. Obviously, the probability is expected to be higher for very low thicknesses (crystals from one to four cells thick, as shown in Fig. 13), but such ideally thin foils are, in practice, either inobservable or at least not representative of the bulk state, due to contamination or perturbation caused by probable atomic relaxations.

Thus it is concluded that the good agreement between the experimental contrast of the defects and that calculated from the configuration shown in Fig. 1(*c*) (assuming the atomic displacements corresponding to the positions given in Table 1) provides further confirmation of the atomic model around vacancies previously deduced from X-ray analysis of various mullites.

Concluding remarks

The present work was undertaken in order to determine the limits of the HREM technique in the study of the structure of mullite. Mullite 3:2 compounds were examined with the ARM, and the results can be summarized as follows: (1) The atomic imaging of mullite is successful due to the excellent point resolution of the microscope, *viz* below 0·2 nm. (2) Very precise requirements concerning the imaging conditions (defocus value, thickness, beam tilt and astigmatism correction) must be fulfilled in order to allow interpretable imaging of this compound to be made. (3) In extremely thin areas, defects have been observed and consistently discussed in terms of the presence of oxygen vacancies along the O3-type columns; the detection of these defects is possible due to the occurrence of at least 50% of cation displacements from nearest-neighbour *T*- to *T**-type columns. (4) From our observations, it is clear that oxygen vacancies are randomly distributed in the 3:2 compounds studied here.

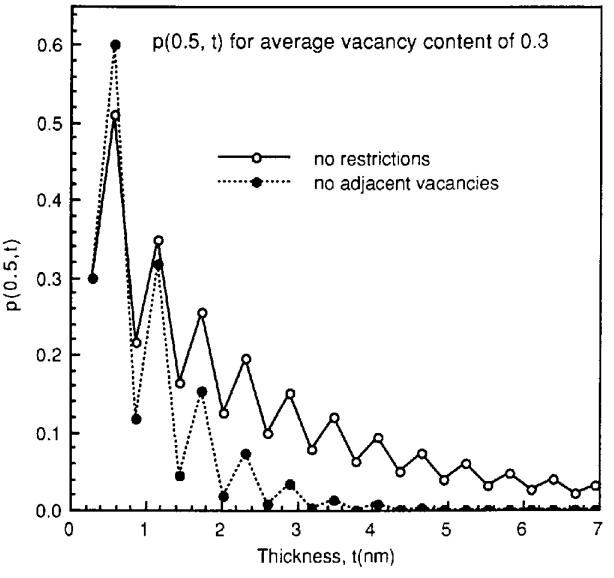

Fig. 13. Probability $p(0{\cdot}5, t)$ as a function of thickness in the case of the *K* mullite (see text). The curve corresponding to a random distribution of vacancies is shown with a full line, and the results obtained with the restriction 'no nearest-neighbour vacancies' constitute the dashed line.

It is a great pleasure to acknowledge the assistance of E. C. Nelson and C. J. D. Hetherington in the use of the ARM, and of R. Kilaas in the computations. Thanks are due to C. Echer and J. Turner for their respective help in analytical microscopy and image processing. We are also indebted to R. Torrecillas (ICV, Madrid, Spain, and GEMPPM, Villeurbanne, France) for providing us with the *T* mullite, and to Kyocera Ceramics for the sintered 3:2 compound. Financial assistance from Mobil Oil Corporation is also acknowledged. Work at NCEM was supported by the Director, Office of Energy Research, Office of Basic Energy Sciences, Materials Science Division, US Department of Energy under Contract no. DE AC-03-76SF00098. The support of NATO in the form of a Research Fellowship to TE is gratefully acknowledged.

References

ANGEL, R. J. & PREWITT, C. T. (1986). *Am. Mineral.* **71**, 1476–1482.

ANGEL, R. J. & PREWITT, C. T. (1987). *Acta Cryst.* **B43**, 116–126.

BURNHAM, C. (1963). *Carnegie Inst. Washington Yearb.* **62**, 158–165.

BURNHAM, C. (1964). *Carnegie Inst. Washington Yearb.* **63**, 223–227.

CAMERON, W. E. (1977). *Am. Mineral.* **62**, 747–755.

EBERHARD, E., HAMID RAHMAN, S. & WEICHERT, H. T. (1986). *Z. Kristallogr.* **174**, 44–46.

EPICIER, T., FUCHS, G., FERRET, P. & BLANCHIN, M. G. (1989). *Philos. Mag.* **A59**, 885–906.

EPICIER, T., THOMAS, G. & O'KEEFE, M. A. (1991). *Acta Cryst.* Submitted.

HAMID RAHMAN, S. & WEICHERT, H. T. (1990). *Acta Cryst.* **B46**, 139–149.

HETHERINGTON, C. J. D., NELSON, E. C., WESTMACOTT, K. H., GRONSKY, R. & THOMAS, G. (1989). *Mater. Res. Soc. Symp. Proc.* **139**, 277–282.

HIRAGA, K., SHINDO, D. & HIRABAYASHI, M. (1981). *J. Appl. Cryst.* **14**, 169–190.

KILAAS, R. (1987). *45th Annu. Proc. EMSA*, edited by G. W. BAILEY, pp. 66–69. San Francisco Press.

KRIVEN, W. M. & PASK, J. A. (1983). *J. Am. Ceram. Soc.* **66**, 649–654.

MCCONNELL, J. D. C. & HEINE, V. (1985). *Phys. Rev. B*, **31**, 6140–6142.

NAKAJIMA, Y., MORIMOTO, N. & WATANABE, E. (1975). *Proc. Jpn Acad.* **51**, 173-178.
NAKAJIMA, Y. & RIBBE, P. H. (1981). *Am. Mineral.* **66**, 142-147.
O'KEEFE, M. A. & BUSECK, P. R. (1979). *Trans. Am. Crystallogr. Assoc.* **15**, 27-46.
SAALFELD, H. (1979). *Neues Jahrb. Mineral. Monatsh.* **3**, 305-316.
SAALFELD, H. & GUSE, W. (1981). *Neues Jahrb. Mineral. Monatsh.* 4, 145-150.
SADANAGA, R., TOKONAMI, M. & TAKEUCHI, Y. (1962). *Acta Cryst.* **15**, 65-68.
SAXTON, W. O., PITT, T. J. & HORNER, M. (1979). *Ultramicroscopy*, **4**, 343-354.
SCHRYVERS, D., SRIKRISHNA, K., O'KEEFE, M. A. & THOMAS, G. (1988). *J. Mater. Res.* **3**, 1355-1361.
SMITH, D. G. W. & MCCONNELL, J. D. C. (1966). *Mineral. Mag.* **35**, 810-814.
SMITH, D. J., SAXTON, W. O., O'KEEFE, M. A., WOOD, G. J. & STOBBS, W. M. (1983). *Ultramicroscopy*, **11**, 263-282.
SPENCE, J. C. H. (1980). *Experimental High Resolution Electron Microscopy*. Oxford: Clarendon Press.
TOKONAMI, M., NAKAJIMA, Y. & MORIMOTO, N. (1980). *Acta Cryst.* **A36**, 270-276.
TORRECILLAS, R. (1987). Unpublished work; thesis in progress.
YLA-JAASKI, J. & NISSEN, H. U. (1983). *Phys. Chem. Miner.* **10**, 47-54.

Acta Cryst. (1990). A**46**, 962-969

Vertex Frequencies in Generalized Penrose Patterns

BY E. ZOBETZ AND A. PREISINGER

Institut für Mineralogie, Kristallographie und Strukturchemie, Technische Universität Wien, Getreidemarkt 9, A-1060 Vienna, Austria

(*Received* 14 *March* 1990; *accepted* 16 *July* 1990)

Abstract

The grid method has been used to calculate the frequencies of the different vertices and corresponding Voronoi polygons occurring in generalized Penrose patterns. A simplified purely geometrical description of the importance of the $\sum \gamma_j = 0 \pmod 1$ relation for Penrose patterns that obey certain necessary matching conditions is given. In n-grids with n odd, local $2n$-fold symmetry occurs only if the inequality $n \cos\alpha/(1+\cos\alpha) \pmod 1 < \sum \gamma_j < n/(1+\cos\alpha) \pmod 1$, where $\alpha = \pi/n$, is fulfilled. n-grids and their corresponding rhombus patterns show global $2n$-fold symmetry if $\sum \gamma_j = 1/2 \pmod 1$, where $\gamma_j = 1/2 \pmod 1$.

Introduction

The theoretical importance of non-periodic tilings arose first from their relevance to questions of mathematical logic. Berger (1966) was the first to discover an aperiodic set consisting of 20 426 Wang tiles (only translations allowed) and therefore refuted Wang's (1961, 1975) conjecture that no aperiodic sets exist. Berger himself (Grünbaum & Shepard, 1987), Knuth (1968) and Läuchli (Grünbaum & Shepard, 1987) were able to reduce considerably the number of necessary tiles. Through a new idea of R. Ammann (Robinson, 1978), 16 is now the least-known number of Wang tiles in an aperiodic set. In 1971, Robinson discovered a set of six tiles (rotations and reflections allowed), which are basically squares with modifications to their corners and sides. Ammann (Grünbaum & Shepard, 1987) described another set of six tiles, which are of similar nature.

Some years ago, Penrose (1974, 1978, 1979) found a pair of rhombi which, when matched according to certain rules (coloured arrows or edge modifications), is forced to tile the plane in a non-periodic way. In both rhombi all sides have length a. The thick rhombus has angles of 72 and 108 ° and the thin rhombus 36 and 144 °. They have areas $A_{\text{thick}} = a^2 \sin(2\pi/5)$ and $A_{\text{thin}} = a^2 \sin(\pi/5) = A_{\text{thick}}/\tau$, where $\tau = (5^{1/2}+1)/2$ ($\simeq 1{\cdot}6180$). In any Penrose pattern the fraction of thick rhombi equals $\tau/(1+\tau)$ and the fraction of thin rhombi equals $1/(1+\tau)$. Therefore, the area covered by thick rhombi is τ^2 times greater than the area covered by thin rhombi.

Two approaches to the analysis and generation of Penrose tilings, the grid method and the projection formalism have been suggested by de Bruijn (1981). These two methods were generalized and extended by Beenker (1982), Kramer (1982), Mackay (1982), Kramer & Neri (1984), Duneau & Katz (1985), Conway & Knowles (1986), Gähler & Rhyner (1986), Levine & Steinhardt (1986), Jannsen (1986), Korepin, Gähler & Rhyner (1988) and Whittaker & Whittaker (1988). Considerable progress in the knowledge of non-periodic tilings has been made during the last few years. For an excellent review the reader is referred to Grünbaum & Shepard (1987).

In the present article, special attention is given to the Penrose tilings and their construction by means of de Bruijn's grid method. The main concern here will be the calculation of the frequencies of the

0108-7673/90/120962-08$03.00